Instability of P-waves below the TR in a 1D solar wind model

R. Grappin[1] J. Léorat[1] R. Pinto[1] and Y.-M. Wang[2]

[1] Observatoire de Paris, LUTH, CNRS, 92195 Meudon, France
   e-mail: `Roland.Grappin@obspm.fr`
[2] NRL
   e-mail: `ywang@yucca.nrl.navy.mil`

ABSTRACT

Aims. Our aim is to investigate the response of the solar atmosphere to perturbations when the transition region and the solar wind flow are included in the modeling.

Methods. We integrate the time-dependent 1D hydrodynamic equations with spherical symmetry and transparent boundary conditions, starting from the photosphere up to 15 solar radii. The model includes conduction, radiative cooling and a prescribed mechanical heat flux. Once a quasi-stationary solar wind is established, we study the response of the system to pressure oscillations of the photospheric boundary.

Results. We find that wavepackets with high enough amplitude propagating upward from the photosphere implode just below the transition region. This implosion is due to the radiative cooling term generating pressure holes close to the wave crests. If we artificially suppress heat sources and sinks, the wave remains stable regardless of its initial amplitude

Conclusions. The instability found here is not an instability of the transition region itself: on the contrary, the instability ceases when the wavepacket enters the transition region where conduction is able to balance the cooling. However, the transition region as a whole can be destabilized by such implosions.

Key words. hydrodynamics – instabilities – Methods: numerical – Sun: transition region

1. Introduction

Among the many decisions to be made before beginning a numerical study of the corona-solar wind dynamics, is where to place the lower boundary; in particular, should the model include the dense cold layers below the corona, or not? Including these cold layers will increase the numerical cost (as the scale height of the cold layers is small). Furthermore, resolving the chromospheric transition region itself will require the increase of the spatial and temporal resolutions there. So, one is tempted not to include the cold layers. The work by Lionello et al. (2001) and by Endeve et al. (2003) shows that interesting results can be obtained in this way, albeit with numerous difficulties.

However, not including the cold layers means not including the transition region in a comprehensive manner, since it is then relinquished to a lower boundary where conditions have to be chosen arbitrarily. Hansteen and Leer (1995) have shown in particular that including the cold layers is essential if one is to recover the observed mass flux in the solar wind. Also, when considering the time-dependent behavior of the atmosphere, the response of the corona to perturbations could depend to a large extent on the choice of these arbitrary boundary conditions. Examples of these effects can be found in the comparison of the results obtained by using the "line-tied" assumption, i.e. a full reflection at the boundary as in the work of Aulanier et al. (2005) and those obtained by using complete transparency, such as in Grappin et al. (2005). More generally, the dynamics of the dense layers could alter the dynamics of the corona and wind. This is demonstrated in the global 1.5D time-dependent solar wind simulations by Suzuki and Inutsuka (2005) (referred to as SI hereafter) and in the work by Gudiksen and Nordlund (2005)

of a 60 x 60 x 37 Mm^3 of the solar atmosphere. Both yield a TR that is erratic both in time and space.

The second question to be considered in the modeling of the solar atmosphere-solar wind system is how to specify the energy equation. The minimal requirement for the energy balance is to include the adiabatic term with $\gamma = 5/3$. If one is not interested in the TR dynamics, then this minimal requirement is acceptable, and one simply starts with a given temperature profile, possibly adding coupling terms in the energy equation to limit the numerical diffusion of the temperature profile. This was done by De Pontieu et al. (2005) in their work on spicules, and to some extent by Del Zanna et al. (2005) in their work on coronal seismology (Velli, personal communication).

However, if one includes heat sources and sinks, it is reasonable to expect that the dynamics will be modified, even for small amplitude perturbations. Currently, the only simulation of the corona and solar wind which includes heat sources and sinks self-consistently, is the one by SI who used 14000 grid points. Clearly such an approach cannot be generalized to 2D or 3D.

Our long-term goal is to devise a reduced version of the SI 1D model, with a reduced number of grid points, e.g. 300 points instead of 14000, thus allowing future generalization to 2D/3D. In the preliminary approach adopted here, we solve the hydrodynamics equations, not the MHD equations, and study the propagation of pressure waves excited at the photospheric level. Since we do not expect plain pressure waves to heat the corona, we use a prescribed mechanical energy flux which is a function of heliocentric distance, such as in Wang (1994). Hence, in comparison to the SI model, our model is not self-consistent. The response of the solar atmosphere to photospheric pressure waves has been studied previously in particular by Fleck and Schmitz (1991) and

Kalkofen et al (1994) in the case of an isothermal atmosphere, and by Cheng and Yi (1996) who take into account the transition region. We compare our work with the latter work in the discussion Section.

We will show that waves excited with high enough amplitude at the base, when arriving in the vicinity of the TR, become unstable to radiative cooling, due to their special phase relations. This may lead them to implode, if their amplitude is too high before entering the TR. This work will demonstrate, at the same time, the feasibility of a time-dependent solar atmosphere-solar wind model starting at the photospheric level with a reduced number of grid points. The equations and the method used are described in Section 2. The results are given in Section 3, followed by a discussion in Section 4.

2. Equations and method

We consider a spherically symmetric solar corona, and solve the time-dependent gas equations, which are given by the equation for the radial velocity:

$$\partial u/\partial t + u\partial u/\partial r + (1/\rho)\partial P/\partial r + GM/r^2 = 0 \qquad (1)$$

Pressure and temperature equations:

$$\partial P/\partial t + u\partial P/\partial r + \gamma P divu = Q \qquad (2)$$

$$\partial T/\partial t + u\partial T/\partial r + (\gamma - 1)T divu = Q/\rho \qquad (3)$$

where $\rho = m_p n$. The density n is deduced from the pressure and temperature, using the equation of state:

$$P = 2nkT \qquad (4)$$

T being the average temperature of ions and electrons.

Before specifying the non-adiabatic source term Q, let us recall some main points on waves, that is, linear solutions of the previous equations, in the simplest case, that is, only adiabatic terms, and a uniform atmosphere. Recall first that the ability of 1D pressure oscillations to propagate or not along the pressure gradient, depends on the frequency being larger or smaller than the cut-off Lamb frequency:

$$\omega_L = c/(2H) = \gamma g/(2c) \qquad (5)$$

c being the sound speed, g the gravity, H the pressure scale height. When propagative, waves have their energy flux about constant in the limit of high frequencies. When evanescent, all the atmosphere oscillates in phase. A first remarkable property of the response of an infinite atmosphere to base perturbations, as shown by Fleck and Schmitz (1991) and Kalkofen et al (1994), is that, when exciting the base with frequencies lorwer than the cut-off, long-lived transients with the cut-off frequency dominate the spectrum in a large part of the atmosphere except in the very lower layers. This was proposed to be a possible explanation for the observed prevalence of 3-min oscillations in chromospheric lines, although Carlsson and Stein (1997) have later shown that, to explain the chromospheric oscillations, one should include radiative transfer.

A second important property, which will be invoked in the discussion, is that progressive waves close to the cut-off frequencies differ from their homogeneous counterpart in several respects. First, in view of the energy density conservation, the velocity amplitude increases exponentially with altitude as $1/\sqrt{\rho_0} = exp^{z/(2H)}$, as well as the relative density fluctuation, and the relative temperature fluctuation. When propagative

($\omega > \omega_L$), the oscillating part of the wave has a real wavenumber which is

$$k = \sqrt{\omega^2 - \omega_L^2} \qquad (6)$$

Most importantly, there are phase differences between the velocity, density and temperature fluctuations: when propagating upward, the temperature is leading the velocity fluctuation, the density is lagging behing. More precisely, if the solutions are of the form:

$$\delta u/c = (A/\sqrt{\rho_0})sin(kz - \omega t)$$
$$\delta\rho/\rho_0 = (A/\sqrt{\rho_0})sin(kz - \omega t + \phi)$$
$$\frac{1}{\gamma - 1}\delta T/T_0 = (A/\sqrt{\rho_0})sin(kz - \omega t + \psi) \qquad (7)$$

then the phase shifts are:

$$tan(\phi) = 1/(2kH)$$
$$tan(\psi) = -1/(4kH) \qquad (8)$$

We now specify the non-adiabatic source term Q in eq. 3 is given by either one of the two following models.
(a)the "full model" including heat sources and sinks:

$$Q = -(\gamma - 1)(divF_m + \rho^2\Lambda(T) + divF_c) + \kappa_1 T" \qquad (9)$$

where F_m, $\Lambda(T)$, and F_c are the (prescribed) mechanical energy flux, the radiative cooling term and the conductive flux, and $\kappa_1 T"$ provides a filtering of the temperature, with $T"$ being a second order derivative weighted by the local mesh Δr: $T" = \partial^2 T/\partial r^2(\Delta r/ < \Delta r >)^2$, $< \Delta r >$ being the average mesh.
(b) the "relaxation model" including as the only non adiabatic term a small smoothing term:

$$Q = \kappa_1(T" - T_0(r)") \qquad (10)$$

where $T_0(r)$ is a prescribed temperature profile, defining the TR. In both the full and the relaxation models, the coefficient κ_1 is small enough, so that its characteristic time scale is much longer than the time scale of the phenomenon studied.

The prescribed phenomenological mechanical flux which leads to global coronal heating is

$$F_m(r) = \hat{e}_r F_m^0(R_s/r)^2 exp\left((R - R_s)/R_H\right) \qquad (11)$$

A typical value for the energy flux is $F_m^0 = 10^5 erg/cm^2/s$, and the characteristic scale for energy dissipation is $R_H = R_s$. The radiation loss function $\Lambda(T)$ is a rough fit to the one by Athay (1986). More precisely:

$$\Lambda(T) = \Lambda_{max}10^{-(log_{10}(T/T_M))^2}f(T) \qquad (12)$$

with peak value $\Lambda_{max} = 10^{-22}$ or $10^{-21}cgs$ (see Table 1), for a temperature $T_M = 0.2MK$. The factor $f(T)$ if 0 for temperatures lower than a threshold $T_\star$, unity for temperatures larger than $2T_\star$, and varies linearly in between. The threshold temperature is set to:

$$T_\star = 0.01MK \qquad (13)$$

The curve corresponding to eq. 12 is given in Fig 1, together with an empirical cooling function taking into account radiative transfer, which is discussed later in the conclusion.

The conductive Spitzer-Harm flux is

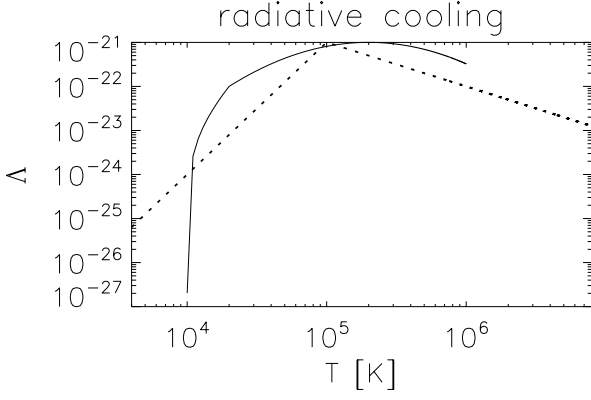$$F_c = -\hat{e}_r\kappa_0 T^{5/2}\partial T/\partial r \qquad (14)$$

Fig. 1. Implemented cooling function (solid line), and empirical cooling function of McClymont and Canfield (1983) (dotted line), discussed in the conclusion.

Run	time	F_m^0	Λ_{max}	κ_0	τ_{lim}	N
S1	0,20	410^4	10^{-21}	10^{-6}	10^{-6}	300
S2	20,40	910^4	10^{-22}	10^{-6}	10^{-7}	300
S3	40,60	910^4	10^{-22}	10^{-6}	10^{-7}	300
D1	60,70	910^4	10^{-22}	10^{-6}	10^{-7}	599

Table 1. List of runs leading to a stationary corona and wind, with heat and source coefficients. Runs S1, S2, S3, D1 follow each other. S1 and S2 respectively correspond to the two phases mentioned in the text. S3 is almost identical to S2 (only the viscous terms differ). D1 starts from an extrapolation of run S3 to a more refined mesh and then relaxes. Time: beginning and end time of each phase; F_m^0: base mechanical flux; Λ_{max}: maximum of cooling term $\Lambda(T)$; κ_0: conductivity parameter; τ_{lim}: characteristic time defining the attenuation of the conductive flux; N is the resolution

where $\kappa_0 = 10^{-6} cgs$. This value lies between the conductivity for the protons and electrons. This form being highly demanding in computer resources (and mesh size), we reduce the steepness of the resulting flux in two ways. First, we use a linear temperature dependence for conductivity at temperature lower than 0.25 MK and pass progressively to the Spitzer-Harm 5/2 power law between 0.25 MK and 1MK (see Linker et al. (2001) for a similar prescription). Second, we limit the resulting flux by requiring that the associated characteristic time $\tau_\star$ be not smaller than a prescribed value τ_{lim}. The final form of the heat flux is thus:

$$F_c = -\hat{e}_r \frac{2}{7} \kappa_0 \frac{\partial T^{N(T)}}{\partial r} (1 + \tau_\star/\tau_{lim})^{-1} \qquad (15)$$

with $\tau_\star = \kappa_0 T^{N(T)-1} (\pi/\Delta r)^2/\rho$ and Δr is the local mesh size, and where the exponent N(T) is expressed in terms of $n_1 = 2$, $n_2 = 3.5$, $T_a = 0.25$, $T_b = 1$ as:

$$N(T) = \frac{n_2 + n_1}{2} + \frac{n_2 - n_1}{2} sin(\frac{\pi(T - 0.5(T_a + T_b))}{T_b - T_a}) \qquad (16)$$

Note that the limiting factor is really reducing the flux only when τ_{lim} is larger or equal to 10^{-6}. As seen in Table 1, this means that in practice the limiting factor is inactive for all runs except run S1.

We use a non-uniform mesh with 300 points following a logarithmic progression of ratio q=1.025. This corresponds to a minimum mesh size being $\Delta r = 10^{-4} R_s = 70$ km at the surface, and a maximum mesh $\Delta r = 0.4 R_s$ at the outer boundary ($r = 15 R_s$). Our temporal scheme is Runge-Kutta of order 3; the spatial scheme is a compact finite difference scheme of order 6 (Lele, 1992) modified to be able to cope with non-uniform grids (J.-M. Le Saout 2003, Grappin et al. 2005). Note however that to compute the temperature gradients which appear in the conductive term, we use a scheme or order two, which is more stable. Finally, we use 6-th order filtering, also defined in Lele (1992). Filtering is used in several places. It is used for the velocity field (roughly once every 10 time steps), and for smoothing different quantities before computing the right-hand sides of the equations. Specifically, the (logarithmic) gradients of pressure, density and temperature are systematically filtered; finally the r.h.s. of the velocity equation is filtered: the latter considerably increases the stability of the schema. Time-step is automatically adapted to the different terms, using a priori estimations of the characteristic times.

Runs	energy	τ	τ_0	ev/prop	amplitude	N
A1	no (1)	6 min	7.6 min	prop	0.4 m/s	300
A1a	no (1)	6 min	7.6 min	prop	1.3 m/s	300
A2	no (1)	11 min	7.6 min	ev	4 m/s	300
B4	yes	10 min	6-8 min	ev	4m/s	300
B40	yes	10 min	6-8 min	ev	40m/s	300
B40a	yes	3 min	6-8 min	prop	40m/s	300
C40	no(2)	10 min	6-8 min	ev	40m/s	300
C400	no(2)	10 min	6-8 min	ev	400m/s	300
D40	yes	10 min	6-8 min	ev	40m/s	599
D80	yes	10 min	6-8 min	ev	80m/s	599

Table 2. List of runs with wave injection. runs A1, A2 start injecting waves at time t=0; other runs start from a relaxed wind flow. Runs Bxx, Cxx start from run S3, runs Dxx start from run D1 (see above Table 1). Energy: yes means energy equation is present; no(1) means coupling of temperature with step-wise constant profile; no(2) means coupling temperature with the stationary profile resulting from integrating the full energy equation. τ and τ_0 are respectively the period of the injected wave and the cut-off period of the dense layers. Ev/prop: ev means evanescent in dense layers, prop means propagative in dense layers. Amplitude is the base amplitude of the wave. N is the number of grid points.

The boundary conditions are imposed via the characteristic form of the equations. They are: no incoming perturbation at the inner boundary, and, starting with time t=1, a constant depression at the outer boundary, introduced via the ingoing characteristics. This depression stops as soon as the sonic Mach number is reached, since thereafter no incoming signal can progress into the domain from the exterior.

Units used in the following are the solar radius for distance, MK for temperature, and km/s or m/s for velocity. Time indicated in figures and tables is mostly measured in numerical unit, which is 1h30. The list of runs building the stationary corona and wind is given in Table 1, a liste of runs in which we perturb the atmosphere with waves injected at the base is given in Table 2.

3. Results

3.1. Wave transfer in a relaxation model

We first consider here the simplified energy equation eq. 10, to check that we recover basic wave properties in a simple configuration. We take for the reference temperature $T_0(r)$ a hyperbolic tangent profile, the low temperature being $T = 0.01 MK$ and the coronal temperature $T = 1MK$. The TR lies at about $R = 0.015 R_s$. Apart from that, the parameters are the same as

for the full wind model: domain size $L = 14R_s$, base density is $10^{17} cm^{-3}$, and same grid. Figure 2 shows the density and temperature profiles (left). In the right panel, we show the profiles of the (square root of the) energy flux, which result from injecting a monochromatic wave starting at time t=0 at the base. The frequency is slightly above the chromosphere cut-off frequency (run A1, Table 2). Hence the quantity plotted should be approximately invariant, except for reflections, due possibly to the frequency being too low in the cold region, and most certainly to reflections at the TR. The sudden energy flux decrease after $R = 1.1R_s$ is due to the filtering, which can be made lighter, so that the damping distance is increased. Filtering should certainly be decreased in view of the future sef-consistent heating of the corona by wave dissipation.
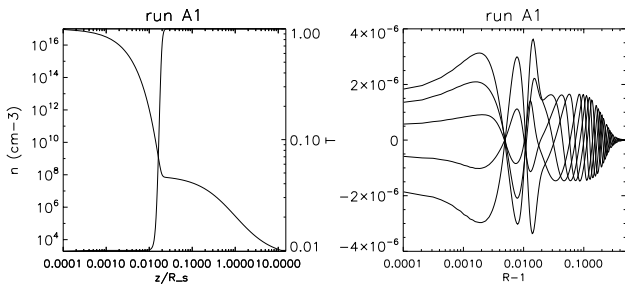

Fig. 2. Waves in a two-temperature atmosphere (relaxation model): Left: density (thick line) and temperature (solid line) profiles; Right: run A1, waves with frequency above cut-off, profiles of $(\rho r^2 v_g)^{1/2} u$ in a the (1,1.5) distance range.
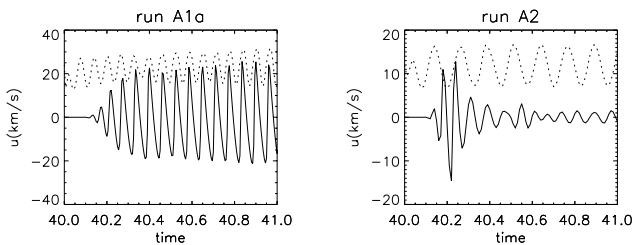

Fig. 3. Oscillations at TR with a two-temperature atmosphere: velocity at TR versus time (dotted: base velocity); left: run A1a, propagative incident wave with a period of 6 min (below cut-off period = 7.6 min.); right: run A2, evanescent waves with period 11 min.

We compare in Figure 3 the velocity response of the TR to waves respectively above and below the cut-off (runs A1a and A2). The signal at the base is shown as dotted points. One sees that injecting high frequency waves at the boundary generates TR oscillations at the same frequency, while low-frequency oscillations at the base generate TR oscillations close to the cut-off frequency (period about 7.6 min). In the latter case, note also that the TR response is not uniform: it is largest during the first two or three periods. Such a dependence of the atmospheric response to the frequency of base excitations has been studied by Fleck and Schmitz (1991) and Kalkofen et al. (1994), as mentioned in the introduction. Here, we concentrate on the TR response, but the oscillation patterns just mentioned are in fact found in a large

part of the atmosphere below the TR, that is, not immediately above the base.

3.2. Generation of the full wind model

We give here an account of the method used to generate the wind and hot corona. We start with an atmosphere at a uniform temperature of $6000K$, and the corresponding hydrostatic equilibrium. The initial hydrostatic stratification is too strong to start immediately to integrate the whole set of fluid equations, essentially because the density is very low at the distance of $R = 15R_s$, which leads to very small characteristic times. We thus first raise substantially the temperature atmosphere before integrating the full equations. This is done during a time limited to $t \leq 1$: we integrate only the temperature equation (either with the full energy terms or the plain relaxation term, depending on the model), and the equation of hydrostatic equilibrium to obtain the pressure. We then use the equation of state to deduce the density from pressure and temperature.

After this short hydrostatic heating phase, we integrate the full equations. As stated above, we apply a depression at the outlet, which forms the transonic wind after some time. When using the full heat sources and sinks, we use successively two sets of parameters (see runs in Table 1). The aim is to approach a density close to $n = 10^8 cm^{-3}$ where the temperature reaches $T = 0.5MK$. The first set of parameters (run S1) leads to a density slightly below this value (see fourth panel in fig 4); the second set (all other runs) achieves the desired result. Note that the first choice of $\tau_{lim} = 10^{-6}$ (run S1) limits somewhat the conductive flux, but that the second value (other runs) leads to no limitation at all. Figure 4 shows several profiles defining the final wind (with set number 2), as well as (bottom right panel) the two temperature/density curves obtained with both sets. A TR is seen to occur at about 0.01 $R_s = 7\,000$ km. The temperature has a minimum about 6000 K at the bottom, and a maximum around 1.6 MK, around 4 solar radii. The chromospheric temperature curve is a smooth ramp, leading to a temperature close to 10000 K at the foot of the TR. This ramp is due to the artificial diffusive term included in the temperature and pressure equations (3) to (5). The sonic Mach number is reached at about 5 solar radii. Note that the heat sources and sinks balance each other (bottom left panel): conductive heating and radiative loss balance at the TR, while conductive loss and mechanical heating balance (with the help of the adiabatic cooling, not shown) in the corona.

3.3. Wave transfer in the full wind model

We now inject waves at the base of the previous stationary atmosphere. We start from the relaxed wind (run S3) with density about $10^8 cm^{-3}$ where the plasma has temperature $T = 0.5MK$ (see figure 4).

We consider as in Section 3.1 monochromatic waves: the velocity is given a sinusoidal pattern, after a transient of a half period. We consider evanescent waves, and return back to propagative acoustic waves only in the discussion. The base period is fixed to be $\tau = 10$ min. Since the cut-off period in the chromosphere is between $\tau_0 = 6$ min (base value) and $\tau = 8$ min (just below the TR), this implies that the wave is evanescent everywhere in the dense layers. The base amplitudes are either 4m/s or 40m/s. Top panels in Figure 5 show the low amplitude, the bottom panels the high amplitude.

In both runs, the oscillations below the TR adopts as previously in the relaxation model a main period of 6 min. (fig. 6).
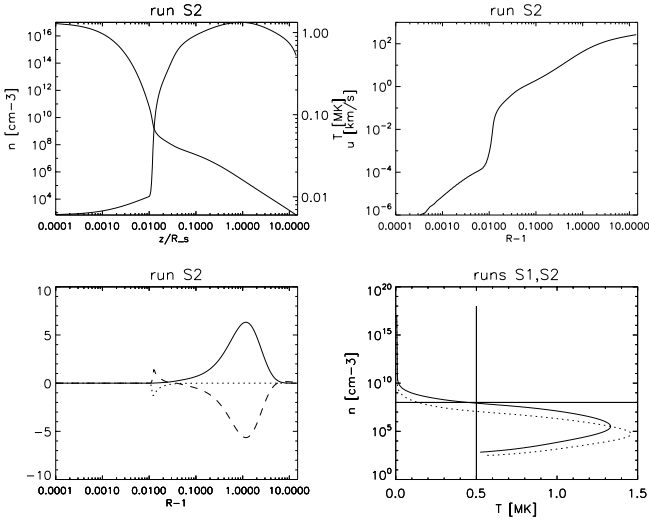
Fig. 4. Stationary transonic wind with full heating sources and sinks (end of run S2, see Table 2). Top left: density and temperature; top right: velocity; bottom left: mechanical heating source (thick line), radiative cooling term (dotted), conductive term (dashed line); note sources and sinks are as they appear in the temperature equation. bottom right: density versus temperature, run S2 with thick line, run S1 with dotted line.

Fig. 5. Evanescent waves propagating through the full wind model. Top: run B4, base amplitude 4 m/s (time interval (60,60.5)); bottom: run B40, base amplitude 40 m/s (time interval (60,60.25); left: velocity profiles weighted by density and sound speed ($\sqrt(n)uc_s$); right: temperature profiles. Note run B40 stops after time $t = 60.3$ (see next figure).

This period is actually the base cut-off period, which means that the wave which reaches the TR is actually just above cut-off in the chromosphere, that is, propagative. The dotted fluctuations (not at scale) show the base velocity fluctuations in both runs, for comparison.

Note that a peculiar behaviour of density and temperature is observed at the base: a transient systematic drift is superposed on the fluctuations. This drift modifies the mean gradients near the base, and allows the atmosphere to solve the contradiction imposed by the incoming characteristics which have in-phase fluctuations of velocity, temperature, density, while upward propagating eigenmodes have phase-lags between the different quantitites.

Run B4 shows two phases, one with about three large oscillations, while the rest of the fluctuations is of much smaller amplitude. Run B40 – with the largest amplitude – stops before the second phase begins, because the profiles become too stiff for the numerical setup after the last temperature minimum, that is, after 60.25. (Although the calculation still proceeds up to time t=60.3, the time interval between 60.25 and 60.3 is unphysical, being invaded by numerical noise). Note the prominent nonlinear features of the large amplitude run: sawtooth velocity pattern, and peaks for the temperatures maxima, large temperature troughs.

The ultimate numerical catastrophy which ends up run B40 results from the inability of the spatial scheme to cope with too large and/or steep velocity/temperature/density profiles which occur when we increase the base amplitude of the wave. The question is : does this numerical catastrophy just reveal the limits of the numerical scheme or does it also reveal a true physical instability of the plasma?

Two remarks are here in order. First, the code is actually able to treat "ordinary" high-amplitude shocks, as we will see in the next subsection. Second, the present high-amplitude waves are growing faster than expected with altitude since, when the base amplitude goes beyond some threshold, the TR amplitude grows faster than proportional to the base amplitude. Indeed, if we look
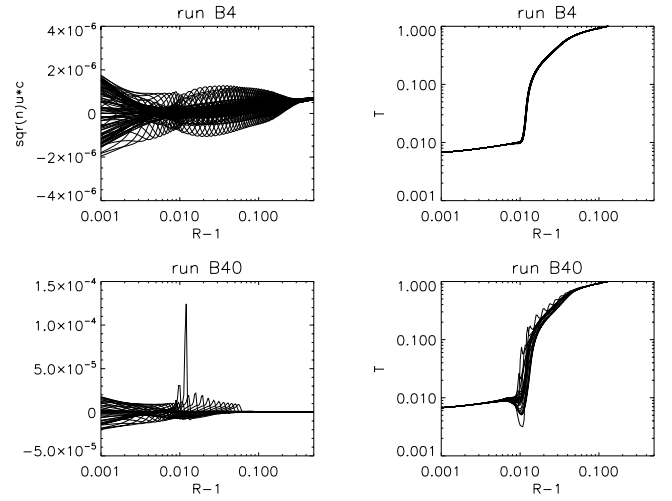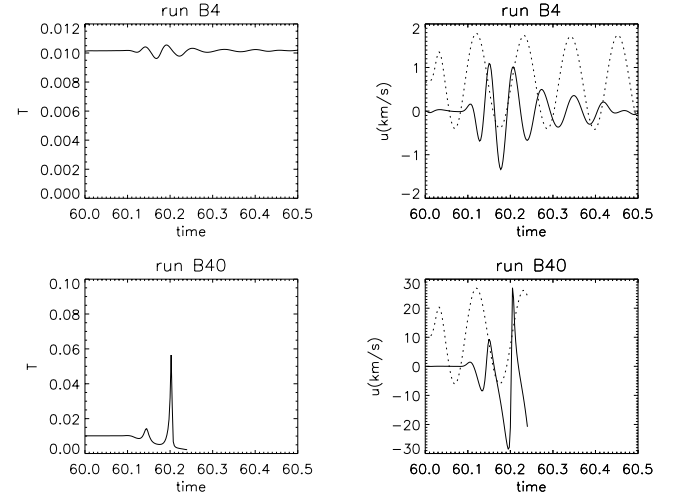

Fig. 6. Evanescent waves propagating through the full wind model. Temperature and velocity at TR versus time; dotted: base velocity; top: run B4; bottom: run B40

at the third extremum in figure 6, at a stage where the numerical description is everywhere correct in both runs, we see that the velocity maximum in run B4 is about 1.5 km/s, while in run B40 it is about 25 km/s: the amplification factor is thus larger than the factor 10 which relates the base amplitudes. So the hypothesis that the phenomenon we see is a true physical instability deserves to be examined in detail.

3.4. Relaxation model again

To see whether the result is generic or not, we now replace the energy equation by the plain temperature equation with a coupling to a given temperature profile, as already considered in section 3.1. In other words, we return to the relaxation model. However, we start now from run S3, which has its temperature profile obtained through the full energy equation. Hence, the dif-

ference with the runs just discussed in the previous subsection is that only the adiabatic terms will react to the impinging wave, since the energy terms are not present. But, again, the starting TR structure will be the same.

Recall that the extra coupling term in the temperature equation is of the form $-\kappa(T - T'')$ (eq. 3). We insist that κ is a small parameter, which, in practice, gives this term a value which is never larger than 20% of the physical conductivity, hence it should not substantially modify the growth rate of the instability, if it is there.

The result, as shown in top of Figure 7, shows that now the large amplitude wave (same as B40) arriving at the TR remain stable (run C40, top panels): the TR oscillations are actually much smaller than previously. Most importantly, when we increase the amplitude again by a factor 10 (run C400), we still obtain a stable TR, with shocks propagating in the high corona (figure 7, bottom panels).
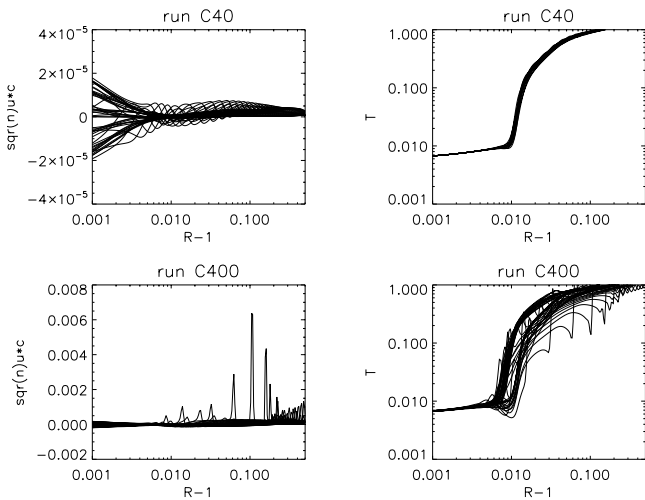

Fig. 8. Evanescent waves, full energy equation, double resolution; temperature and velocity at TR versus time; top: run D40, base amplitude 40m/s; bottom: run D80, base amplitude 80m/s. Compare run B40, Figure 6.

Fig. 7. Evanescent large-amplitude waves without energy terms, coupling with stationary temperature profile. Top: run C40, base amplitude 40 m/s; bottom: run C400, base amplitude 400 m/s left: velocity profiles ponderated by density and sound speed, $\sqrt{(n)}uc_s$; right: temperature profiles.

Fig. 9. Evanescent waves, full energy equation, double resolution; successive profiles of temperature (top), velocity (middle) and cooling term as in eq. (3) and (6) (bottom), in the vicinity of the TR during time interval 70.125 and 70.15 (waves propagate rightwards); left: run D40, base amplitude 40m/s; right: run D80, base amplitude 80m/s

4. Discussion

We have found that the response of the TR to impinging transient evanescent waves varies strongly, depending on whether extra-adiabatic terms are present or not. The instability observed in the former case is nonlinear, that is, it shows up apparently only when waves have a sufficiently high amplitude.

To establish more firmly the physical status of the instability, we redo the experiment with large amplitude wave (B40), but now with double resolution, dividing each mesh in two parts. Asking for the same domain size, we thus end up with $N = 599$ grid points instead of $N = 300$.

The calculation is now stable, as shown in top of figure 8 (run D40). To recover the instability, we must increase the base amplitude by a factor two (run D80, bottom figure). It is interesting to examine in detail the two successive phases in run D40 (the stable one), because they show all characteristics of run B40 (nonlinearities), but during a longer time, since it escapes numerical catastrophe. During the first (nonlinear) phase,
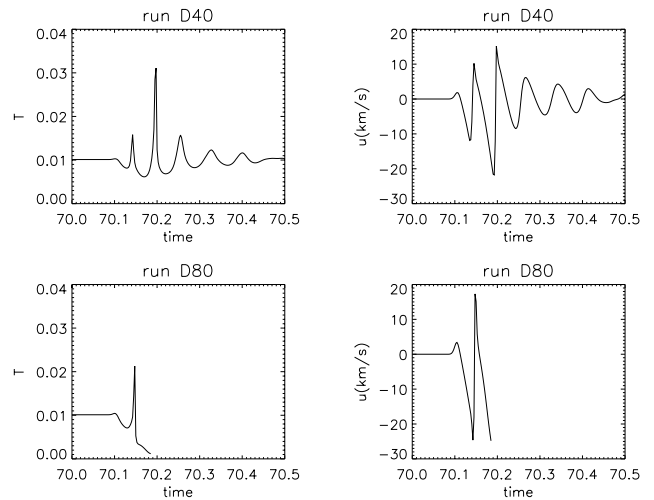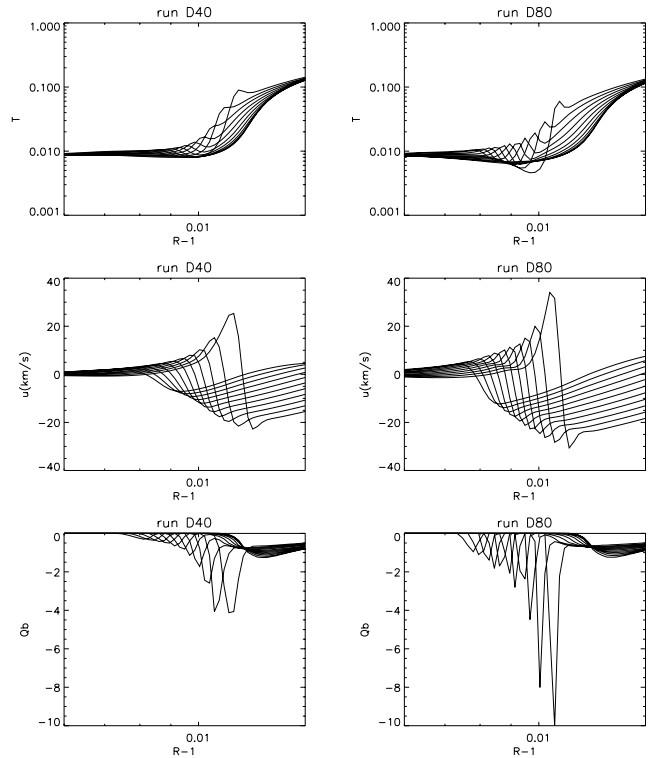
temperature and velocity are very different: temperature shows symmetric spikes (only for maxima), while velocity shows sawtooths. During the second phase (which doesn't exist for run D80), one finds ordinary quasi-monochromatic oscillations of smaller amplitude for both fields. The early velocity sawtooth pattern reveals shock formation, while the spiky appearance of

the temperature pattern reveals the (nonlinear) advection of the temperature "wall" by the velocity field. There is a last (crucial) feature shown by temperature, that is, the steady increase of the temperature troughs, which disappears in the second phase for run D40, and finally leads to the end of run D80.

In fact, it seems that B40 is very close to run D40, the only difference being that D40 is able to pass the critical phase with the largest fluctuations, and not B40. So, we can safely conclude that, while this difference is due to resolution change (and associated filtering change), the early nonlinear large response of the TR to upward propagating waves is physical, i.e., not due to the details of the spatial scheme.

Note that the observed instability has an amplitude threshold, but that the response probably depends on the incoming perturbation being transient, as the spectrum is changing with time after starting the injection (the signal is not purely monochromatic, beginning at a finite time). Note also that the most striking difference between the low amplitude run (run B4) and the higher amplitude run (B40), as shown in figure 5 and also figure 6 is the appearance of large cold troughs at the foot of the TR.

While the temperature peaks (see figure 6 or figure 8) can be attributed to the (nonlinear) advection of the TR temperature "wall" by the large velocity fluctuations, what is the origin of the (growing, unstable) temperature troughs? We propose that the cause both of the growth of the cold troughs is the radiative cooling term. This has the immediate advantage of explaining the nonlinearity of the response to the wave base amplitude. Indeed, the cooling term dependence on temperature is very nonlinear in the low temperature range (see section 2), with a cut-off at $10^4 K$ (eq 13).

Here is the detailed scenario we propose. Consider the upward propagating wavefront resulting from a perturbation at the base, for instance the beginning of our monochromatic injection. During its propagation upward, it steepens progressively, but the as altitude increases, its amplitude is growing due to the approximate energy density conservation, so that the steepening rate is increasing also.

If the wave was submitted only to the usual adiabatic processes, then it would proceed as just said: propagating, growing, steepening. But there are extra terms in the energy equation. The conductive term is definitely negligible below the TR, as well as the mechanical flux term. Note that the radiative cooling term remains strictly zero, but only as long as the temperature remains below the threshold (here $10^4 K$, eq. 13).

Hence, this remains so all the way up to the TR, if the initial amplitude of the wave is small enough for the threshold $T\star = 10^4 K$ not to be trespassed during propagation. But, in the opposite case, then the wave crest is cooled immediately, with a rate proportional to the local density of the plasma. Hence the temperature maxima of a large amplitude wave will be cooled both sooner (at lower altitude) and more rapidly than a small amplitude one.

What is the effect of the temperature drop when the wave crest is cooled down? Before answering, let us examine in detail the growth of the instability in more detail. Figure 9 shows for runs D40 et D80 10 successive profiles at early times, from time t=70.125 to t=70.15, of temperature, velocity and cooling term in the vicinity of the TR. The time interval corresponds to the first large oscillation at the TR, as seen in figure 8. It is seen that the growth of the cooling term and the growth of the temperature and velocity wavefront go together. Recall that both the conductive and mechanical heating terms are negligible in the region discussed, as stated above.
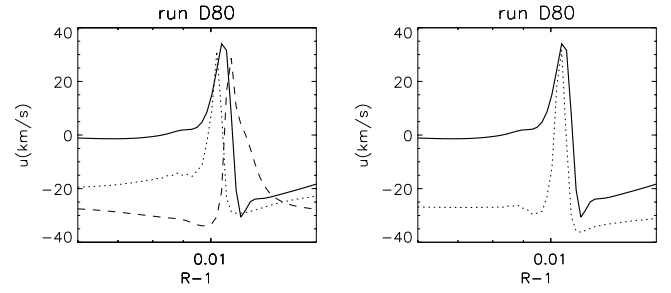

Fig. 10. run D80: Instantaneous profiles of velocity, density, temperature and pressure at t=70.15; left: velocity (thick line), density fluctuation (dotted), temperature fluctuation (dashed line); right: velocity (thick line), pressure fluctuation (dotted)

Now, the effect of the radiative cooling depends critically on the phase relations between the different degrees of freedom. In the case of a purely progressive acoustic wave propagating in a homogeneous medium (no gravity), with all fluctuations in phase, the radiative cooling would only lead to damping.

Actually, the density, pressure, and velocity of our waves are almost everywhere not in phase. This is seen in figure 10 which shows in detail the different profiles at the last time of the series shown in figure 9. The left panel shows that the temperature crest is leading the velocity crest, while the density crest lies behind it. As the temperature crest is decreased by the radiative cooling, this decreases the right foot of the pressure bump, which accelerates the fluid ahead of the wave toward the pressure drop. This in turn raises the pressure, hence raises again the temperature above the threshold, etc... This unstable growth stops when the wave paquet enters the TR. This is because in the TR, conductive terms become important, and are able to balance cooling, so the instability stops. Hence, the instability is that of the high chromospheric layers, where conduction is not able to balance radiative cooling of large-amplitude waves.

We have dealt up to now with the case of evanescent waves. We now redo the previous runs with an injection frequency lareger than the cut-off, e.g. an injection period of $\tau = 3min$ (run B40a). A main difference (as in the case of the given TR, see figure 3) is that the TR oscillations adopt the injection period, that is, the long-lasting transient response of the atmosphere no longer dominates. More importantly, the same phase shifts between degrees of freedom as in the lower frequency case are observed, and the amplitude threshold for instability is about the same.

Note that, in principle, frequencies high enough compared to chromospheric cut-off should have all degrees of freedom in phase, and so, presumably, should remain stable whatever their amplitude. We couldn't check that this is true in the present model, as waves with significantly higher injection frequencies (say, a period of 1 or 2 min suffer from too high damping during their propagation through the TR so that the cut-off frequency is again dominant there, which implies that the wave is again unstable. A possible way to check the high-frequency stability should thus imply either increasing resolution or changing the filtering algorithm.

Our results should be compared with those by Cheng (1992) who studied the response of the chromosphere to pressure waves, using a similar energy equation, in particular, an optically thin expression for the radiative cooling function. This author does not find the waves to be unstable. It is not easy to determine whether the amplitude he considers is comparable or not to the

threshold amplitude around 40m/s found here, however, since this author considers quasi-impulsive perturbations. Cheng and Yi (1996) further considered the radiative loss due to emission lines in the chromosphere, instead of the optically thin limit. In this paper, the authors considered continuous perturbations wich a rich spectrum, with amplitudes comparable to the amplitude considered here. In both cases, the authors don't mention anything like the instability of the progressive waves which we have studied here.

To check to some extent, whether the thermal instability found here is dependent on the particular choice of our cooling function, we considered the cooling function advocated by McClymont and Canfield (1983). These authors suggest replacing the cooling function (12) by the following term:

$$\Lambda(T) = \Lambda_{max}((T/T_M)^m - (T_0/T_M)^3) \qquad (17)$$

where $T_M = 0.1 MK$, m being 3 if $T < T_M$ and -1 if $T > T_M$. The first part of the r.h.s is the cooling term shown as a dotted line in Figure 1 This form of the cooling function has no cut-off at low temperature; the authors report that it gives a good fit to the effective loss function which they find when taking into account the finite optical thickness in the chromosphere. Since there is no cut-off to the cooling term itself, we have to subtract the second term of the rhs of eq (17) which acts as a heating term, and so allows to reach a stationary chromospheric temperature close to a given constant value T_0. Also, in order to limit the characteristic time associated with the new cooling term, which would otherwise grow to very large values at the photospheric base, we limited the square-density dependence in eq. (9) in the following way: $n^2\Lambda(T)$ becoming $n^2 n^\star/(n + n^\star)\Lambda(T)$. With this prescription, the cooling rate becomes density-independent when density is larger than $n^\star$. Note that if we set $n^\star$ close to the TR density itself (typically, $10^8 cm^{-3}$), its very structure will be strongly modified. We have chosen $n^\star = 10^{11} cm^{-3}$, and $T_0 = 0.08 MK$. We have found that, using this alternative model, the growth rate of the TR oscillations in a run equivalent to B40 was not basically changed.

To summarize, we have devised a time-dependent 1D solar wind model incorporating the dense cold layers below the transition region. As a first application of the model we found that wave packets with high enough initial amplitude and propagating upward with frequency in the vicinity of the cut-off frequency implode as they arrive in the upper layers below the TR. This process might contribute among others to peak the oscillation spectrum around the cut-off frequency.

References

Aulanier, G., Démoulin, P., Grappin, R. Astron. Astrophys. 430, 1067 (2005)
Athay, R. G., Astrophys. J. 308, 975 (1986)
Carlsson, M., Stein, R. F., Astrophys. J. 481, 500 (1997)
Cheng, Q.-Q., Astron. Astrophys. 266, 537 (1992)
Cheng, Q.-Q., Yi, Z., Astron. Astrophys. 313, 971 (1996)
Del Zanna, L., Shaekens, E., Velli, M., Astron. Astrophys. 431, 1095 (2005)
DePontieu, B., Erdélyi, R., James, S., Nature 430, 536 (2004)
Endeve, E, Leer, E, Holzer, T, Astrophys. J. 589, 1040 (2003)
Fleck, B. and Schmitz, F., Astron. Astrophys. 250, 235 (1991)
Grappin, R, Léorat, J., Habbal, S. R., Astron. Astrophys. 437, 1081 (2005)
Gudiksen, B.V., Nordlund, A., Astrophys. J., 618, 1020 (2005)
Hansteen, V. H., Leer, E., J. Geophys. Res. 100, 21577 (1995)
Kalkofen, W., Rossi, P., Bodo, G., Massaglia, S., Astron. and Astrophys. 284, 976 (1994)
Lele S.K., J. Comput. Phys. 103, 16 (1992)
Linker, J.A., Lionello, R., and Mikic, Z., J. Geophys. Res. 106, 25165 (2001)
Lionello, R., Linker, J.A., and Mikic, Z., Astrophys. J., 546, 542 (2001)
McClymont, A.N., Canfield, R.C. Astrophys. J. 265, 497 (1983)
Rosner, R., Tucker, W. H., and Vaiana, G. S. Astrophys. J. 220, 643 (1978)
Schmitz, F., Fleck, B. Astron. Astrophys. 260, 447 (1992)
Suzuki, T.-K. and Inutsuka, S., Astrophys. J. 632, L49L52 (2005)
Wang, Y.-M., Astrophys. J. 435, L153 (1994)